

2D Electron Cyclotron Emission Imaging at ASDEX Upgrade^{a)}

I.G.J. Classen^{1,2,b)}, J.E. Boom², W. Suttrop¹, E. Schmid¹, B. Tobias³, C.W. Domier³, N.C. Luhmann Jr.³, A.J.H. Donné^{2,4}, R.J.E. Jaspers⁴, P.C. de Vries², H.K. Park⁵, T. Munsat⁶, M. García-Muñoz¹, P.A. Schneider¹

¹Max Planck Institut für Plasmaphysik, 85748 Garching, Germany

²FOM-Institute for Plasma Physics, Rijnhuizen, 3430 BE Nieuwegein, The Netherlands

³University of California at Davis, Davis, CA 95616, USA

⁴Eindhoven University of Technology, Eindhoven, 5600 MB, The Netherlands

⁵POSTECH, Pohang, Gyeongbuk, 790-784, Korea

⁶University of Colorado, Boulder, CO 80309, USA

(Presented XXXXX; received XXXXX; accepted XXXXX; published online XXXXX)

The newly installed Electron Cyclotron Emission Imaging (ECEI) diagnostic on ASDEX Upgrade provides measurements of the 2D electron temperature dynamics with high spatial and temporal resolution. An overview of the technical and experimental properties of the system is presented. These properties are illustrated by measurements of the edge localized mode (ELM) and the reversed shear Alfvén Eigenmode (RSAE), showing both the advantage of having a 2D measurement, as well as some of the limitations of ECE measurements. Furthermore, the application of singular value decomposition (SVD) as a powerful tool for analyzing and filtering 2D data is presented.

I. INTRODUCTION

Many processes and instabilities in tokamak plasmas exhibit 2D dynamics, thereby making them difficult to diagnose by 1D diagnostics. The strength of 2D ECEI was first demonstrated at the TEXTOR tokamak¹. This diagnostic measured the electron temperature in an 8 (radially) by 16 (vertically) array of sampling volumes, providing a detailed coverage of a section of the poloidal plasma cross section of about 8 by 16 cm in size. It provided valuable physics insight in the research of, amongst others, the sawtooth instability^{2,3} and tearing modes^{4,5}.

Recently an ECEI system has been installed at ASDEX Upgrade in order to investigate the 2D electron temperature dynamics of other reactor relevant instabilities, including edge localized modes (ELMs) and neoclassical tearing modes (NTMs), not easily accessible at TEXTOR. This system images a plasma area of approximately 12 by 40 cm (8 by 16 channels). An overview of the technical and experimental properties of this ASDEX Upgrade ECEI system is presented here. Apart from giving a description of the system (sections II and III), this paper also covers an overview of the experimental ranges and limitations from the perspective of a user (section IV). These properties will be illustrated by measurements of the ELM instability, showing both the advantage of having a 2D measurement, as well as some of the limitations of ECE measurements (section V). Finally, singular value decomposition (SVD) is used to overcome the limitations set by thermal noise, which allowed the visualization of Alfvén waves (section VI).

II. THE PRINCIPLE OF ECEI

A standard (1D) Electron Cyclotron Emission (ECE) radiometer measures the electron temperature at different radial locations along a single line of sight, making use of the magnetic field dependence of the electron cyclotron frequency $\omega_{ec} = eB/m_e$ due to the variation of the magnetic field with major radius $B \approx B_0 R_0/R$ as is seen in figure 1a. In thermal equilibrium, the measured intensity at a given resonant frequency (and corresponding radius) is given by the Rayleigh-Jeans limit of Planck's law $I_{BB}(\omega) = \omega^2 k_B T_e / (8\pi^3 c^3)$, so the plasma behaves as a black body and the intensity is proportional to the electron temperature. Therefore, a frequency resolved measurement of the electron cyclotron emission intensity constitutes a radially resolved measurement of the electron temperature.

The same principle is employed in a 2D ECEI diagnostic, except that multiple lines of sight are simultaneously quasi-optically imaged onto a linear array of diode detectors (see figure 1b). Each of the lines of sight is treated as a 1D ECE radiometer. This gives a direct 2D measurement of the electron temperature; radially resolved due to the frequency resolved measurement of the ECE intensity along each line of sight, vertically resolved due to the multiple lines of sight corresponding to the detectors on the array.

2D ECEI was first demonstrated¹ at the TEXTOR tokamak. This system measured the 2nd harmonic X-mode ECE radiation at 8 frequency bands along 16 lines of sight. An overview of the development of ECEI systems since the first TEXTOR diagnostic can be found in literature⁶. More recently, following cessation of ECEI activities on TEXTOR, the detector array and electronics of

^{a)} Invited paper published as part of the Proceedings of the 18th Topical Conference on High-Temperature Plasma Diagnostics, Wildwood, New Jersey, May, 2010.

^{b)} Author to whom correspondence should be addressed. Electronic mail: ivo.classen@ipp.mpg.de

the final TEXTOR system have been incorporated into the new ECEI system on ASDEX Upgrade, which is the primary subject of this paper.

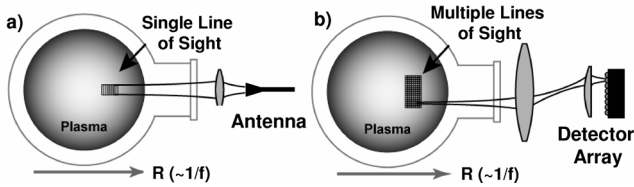


FIG. 1. Comparison between a) a standard 1D ECE radiometer and b) a 2D ECEI system. In an ECEI system, multiple lines of sight are imaged onto a 1D array of detectors.

III. ASDEX UPGRADE ECEI

In figure 2, a schematic representation of the various components of the ASDEX Upgrade ECEI system is given. ECEI uses the same 36 cm diameter quartz vacuum window as the 1D ECE radiometer (‘manhole’ in sector 9), and also shares part of the (newly designed) optics with this diagnostic. The two systems are separated by a beam-splitter (a thin dielectric foil) that has an approximately 50/50% transmission/reflection over the full range of frequencies, with the ECEI optical path in reflection. The ECEI optics actually consist of two branches, the front side optics that images the plasma radiation on the detector array, and the LO side optics (separated from the first one by a further beam-splitter) that images the local oscillator (a backward wave oscillator, BWO) beam on the array. All ECEI components (except the computers) are positioned in the ASDEX Upgrade torus-hall. The various components of the system are described in the following paragraphs.

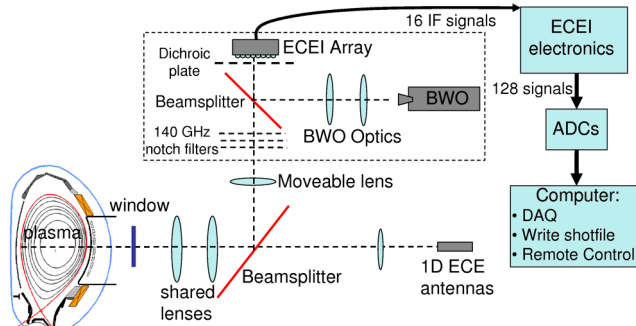


FIG. 2. (Color online). Diagram showing all major components of ECEI.

The ASDEX Upgrade ECEI system utilizes the detector array and IF electronics of the previous TEXTOR ECEI system. The detector array employs 16 dual dipole antennas with an array of 16 miniature elliptical substrate lenses⁹ (minilenses) in front of them, yielding highly Gaussian, parallel field patterns. In figure 3, a schematic layout of the ECEI electronics of a single antenna is shown. The signal is down-converted two times. The first down-conversion occurs at the array, by mixing the plasma signal with the BWO signal (tuneable between 90 and 140 GHz). This is a single side band down-conversion; the lower side band is rejected by using quasi-optical high pass filters (dichroic plates) in front of the array. The down-converted broadband signal of each of the 16 antennas is transmitted to the 16 IF electronic modules by microwave cables.

In the IF modules, the signal is divided into 8 portions, that are subsequently mixed with 8 local oscillator signals (voltage controlled oscillators at $f_{LO}=2.4, 3.2, 4.0, 4.8, 5.6, 6.4, 7.2,$ and 8.0 GHz) in the second down-conversion step. The frequency difference between these local oscillators determines the radial inter-channel spacing of ECEI and is hence 800 MHz. This typically corresponds to 1.5 cm in the plasma, depending upon the gradient of B . The full radial coverage of ECEI is hence approximately 12 cm. The resulting signals are band pass filtered (double sideband), with an intermediate frequency bandwidth B_{IF} of 700 MHz. This determines the frequency bandwidth of the ECE radiation selected by each channel and, along with broadening effects, the radial resolution. After detection, the signals are low pass filtered (with a tenth order filter) with adjustable video bandwidth $B_V=25-400$ kHz, determining the time resolution of ECEI. The sampling frequency is normally set to (at least) twice B_V . Finally, the signals are converted to a digital signal by 12 bit digitizers, capable of storing 2 Msamples per channel at a maximum sampling rate of 2 Msamples/s. More technical details concerning the array and electronics can be found in the literature^{7,8,9}.

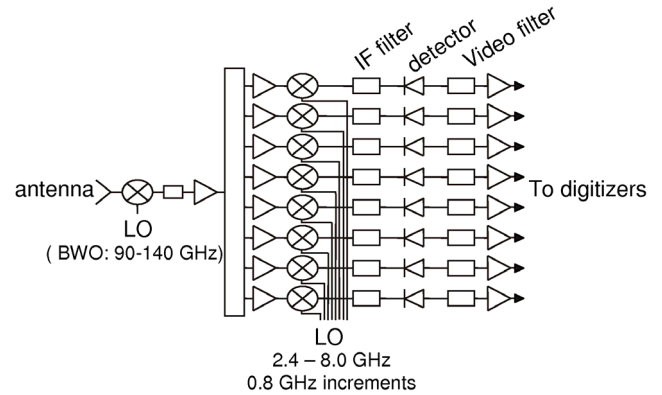


FIG. 3. Schematic representation of the electronics of a single detector for a typical ECEI system.

The front side optics, shown in figure 4, consist of a set of high density polyethylene (HDPE) lenses, part of which is shared with a 60 channel (1D) ECE radiometer. The line of sight of the 1D system is designed to coincide with the optical axis of ECEI, providing in the same poloidal plasma cross section simultaneously a measurement of the full 1D electron temperature profile as well as detailed 2D coverage of a selected area of about 12 by 40 cm (8 by 16 channels). This also makes cross calibration with the absolutely calibrated 1D system easier.

ECEI lines of sight have adjustable (although not independent) foci. This is made possible by translating one of the lenses to shift the position of the focal plane to the desired radius (figure 4). This makes it possible to always operate ECEI in focus (unlike 1D ECE, which has a fixed focus). Also, the confocal parameter (about 40 cm) is larger than the radial coverage, ensuring all ECEI channels are in focus.

The optics have been designed such that the location along the beam path where all 16 beams from the detectors exactly overlap each other in space (the Fourier plane of the optics) lies close to the window aperture. In this way, all beams use as much of the aperture as possible, thereby optimizing the perpendicular spatial resolution. The window aperture is hence the limiting factor determining the (diffraction limited) Gaussian beam waist

$w_0 = 2d\lambda/\pi D$, where d is the distance from the window aperture (1.8 m at the center of the plasma) and $D=0.36$ m is the window aperture diameter (see figure 4). This gives a smallest possible spot size of about $w_0=15$ mm in the plasma, which is also achieved by the optics. The antenna pattern of each of the detectors (including their associated minilens) can be approximated by a Gaussian beam with a waist of 7 mm in the object plane (at the detector), and the array of 16 detectors has a length of 20 cm. The optics images this object plane (array) onto the focal plane in the plasma. Note that the spot size and vertical coverage in the plasma can not be independently imaged. Consequently, the ideal spot size of 15 mm in the plasma (about a factor of 2 larger than the spot size at the array), also fixes the vertical coverage in the plasma, which is about 40 cm (twice the size of the array). Therefore, with the current array, a smaller vertical coverage is not possible (the beams would not fit through the window aperture), and a larger coverage would lead to a proportionally larger spot size.

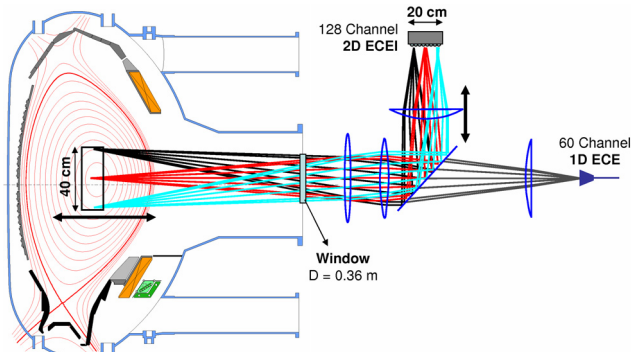


FIG. 4. (Color online). Optics of the ASDEX Upgrade ECEI system. Part of the optics are shared with the 60 channel 1D ECE radiometer. The position of the focal plane can be shifted by translating one of the HDPE lenses.

The local oscillator for the first down-conversion step is a backward wave oscillator (BWO). This is a tunable microwave source that typically delivers a 50 mW microwave beam at an adjustable frequency between 90 and 140 GHz (F-band), with a frequency stability of 0.02%. The BWO optics image the radiation quasi-optically onto the detector array as an elongated Gaussian beam, in order to illuminate all 16 detectors. The BWO is enclosed in a 1cm thick iron casing for stray magnetic field shielding.

The available cut-off frequencies of the dichroic plates for side band rejection are currently 99.1 GHz, 105.0 GHz, 111.7 GHz, 115.6 GHz and 120.2 GHz. The filter has to be chosen such that the lower side band plasma light is blocked, while permitting both the upper side band and BWO frequencies to pass. Therefore, in practice the filter must have a cut-off frequency just below the BWO frequency, thereby limiting the number of useful BWO frequency settings to the available dichroic plates.

Operation during 140 GHz electron cyclotron resonance heating (ECRH) is possible. In order to protect the array against stray ECRH power, three quasi-optical notch filters with a (combined) 60 dB rejection at 140 GHz (3 dB rejection at about 127 GHz) are used. No notch filters are currently available for other ECRH frequencies at ASDEX Upgrade. Operation with a dichroic plate cut-off frequency above the ECRH frequency is

always possible. In other cases, the system will be shielded with a shutter.

The ECEI diagnostic has been designed to be fully remotely controlled. The position of the focusing lens, the frequency and power of the BWO and the selection of the dichroic plates (using a stepper motor controlled slide with 5 filters and a shutter) are all remotely controlled. Also, the system can be switched on and off remotely. No entry to the torus hall is required at any stage during operation, greatly enhancing the flexibility of the system.

IV. OPERATIONAL RANGE AND LIMITS

The range of radii to which ECEI can be tuned to during experiment depends on the toroidal magnetic field and on the frequency range of the diagnostic. Figure 5 provides a graphical representation of this operational range. The horizontal shaded area represents the accessible plasma region (the 2nd harmonic ECE radiation from the HFS is blocked by the 3rd harmonic resonance at the low field side). The tilted shaded area represents the range ECEI can be tuned to as a function of B_0 , limited by the frequency range of the BWO. In reality, not all BWO frequency settings can be used, due to the limited number of available dichroic plates to reject the lower side band. The dark shaded area gives the limitation set by the currently available dichroic plates. Therefore, currently the plasma center is accessible between $B_0=1.8$ T and 2.25 T and the LFS edge between 2.35 T and 2.9 T.

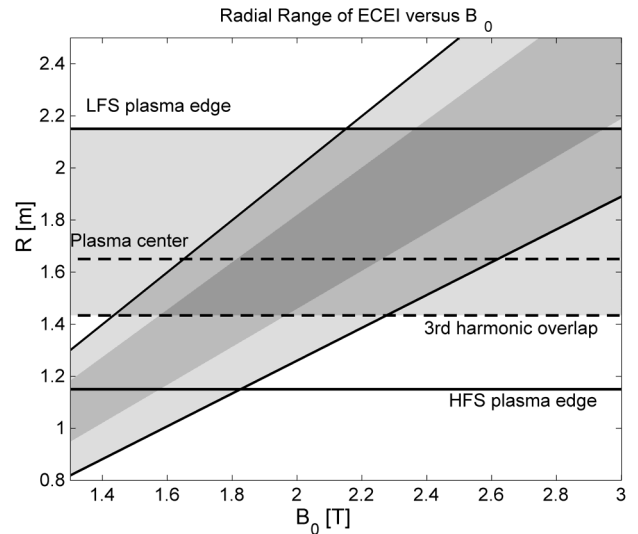


FIG. 5. Range of possible measurement positions ECEI can be tuned to as a function of the toroidal magnetic field B_0 . The darkest shaded area represents the (current) operational range.

Another limitation is set by cut-off. For a 2nd harmonic X-mode ECE diagnostic, cut-off occurs at the right hand cut-off frequency¹⁰

$$\omega_R = \frac{1}{2} \left[\omega_{ec} + (\omega_{ec}^2 + 4\omega_p^2)^{1/2} \right] \quad (1)$$

where $\omega_p = \sqrt{n_e e^2 / (\epsilon_0 m_e)}$ is the density dependent plasma frequency. Figure 6 gives the density above which cut-off occurs as a function of radius and toroidal magnetic field. Note that

measurements at high density generally also require a high toroidal magnetic field. When in cut-off, the 2nd harmonic X-mode radiation can not reach the observer, so signal levels drop towards zero, although some 2nd harmonic O-mode radiation is normally still visible due to the finite sensitivity to O-mode of any real diagnostic. Another related effect to be aware of is the bending of the (mainly off-axis) lines of sight due to refraction. Close to cut-off, the index of refraction of the plasma becomes noticeably smaller than unity which refracts the lines of sight away from the plasma center. This effect rapidly becomes smaller when the plasma is further from cut-off.

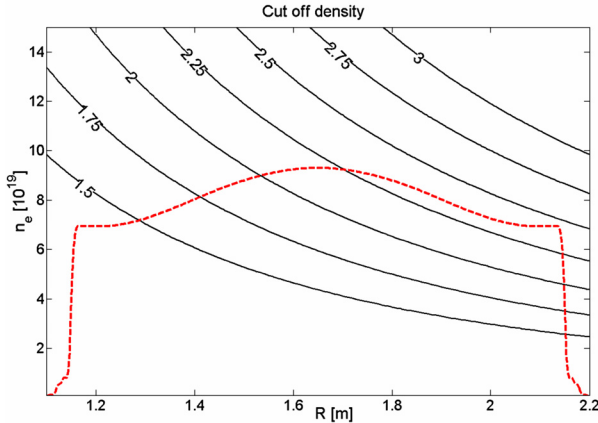


FIG. 6. (Color online). Cut-off density (black, solid) as a function of major radius R for various toroidal magnetic fields B_0 (labels). The dashed red curve gives a typical example of a density profile. In this example, parts of the plasma would be in cut-off for $B_0 < 2.5$ T.

Two other properties of ECE measurements to be shortly addressed are the optical thickness, and broadening effects. The optical thickness for 2nd harmonic X-mode radiation is (for typical AUG parameters $B_0 = 2.5$ T and $R_{resonance} = 2$ m) approximately given by $\tau_{X2} \approx 3.3 \times T_e [keV] \times n_e [10^{19}]$ (see reference 10 for exact formula). If the optical thickness is too low (comparable to or below unity), the plasma is partially transparent and the ECE measurements (the radiation temperature T_R) can no longer be regarded as a direct electron temperature measurement (also density plays a role). Neglecting wall reflections, the radiation temperature is given by¹⁰ $T_R = T_e (1 - \exp(-\tau))$, where τ is a function of both temperature and density. For normal ASDEX Upgrade H-mode plasmas, this only plays a role at the foot of the pedestal (see next section).

The frequency broadening of the ECE radiation due to relativistic effects^{10,11} $\Delta\omega_{rel} \approx n\omega_{ec} (v_{th}/c)^2$ (where $v_{th} = \sqrt{2k_B T_e / m_e}$), and Doppler broadening^{10,12} $\Delta\omega_D \approx 2v_{th}/w_0$ (which for perpendicular observation can be regarded as an effect of the finite transit time of the emitting electrons through the Gaussian spot of size w_0), result in an emitting layer with significant radial extent (for ECEI at 1 keV about 3 cm full width at half maximum). However, in the optically thick case, most of the radiation of the broadened emission layer is reabsorbed before it reaches the observer, and only the last layer (typically narrower than 1cm), closest to the observer, contributes to the ECE signal, and determines the radial spatial resolution. In the optically thin plasma edge (see next section) the full emission layer is observed.

V. 2D DYNAMICS: EDGE LOCALIZED MODES

One of the main motivations for installing ECEI at ASDEX Upgrade was the study of edge localized modes (ELMs), one of the most important and still not fully understood instabilities in fusion devices. The necessity for a 2D diagnostic is illustrated in figure 7, where ECEI measurements of the LFS plasma edge during different phases of an ELM crash are presented. The data have been filtered (using singular value decomposition, see section 6) to reduce the thermal noise. The observed pronounced 2D dynamics would not have been accessible with a conventional 1D ECE radiometer. Figures 7b, c and d are taken during the early stages of the crash (time indicated in figure 7a) where a clear deformation of the temperature profile due to (precursor) mode activity is visible, showing a rather complicated and partly incoherent poloidal mode structure. In figure 7, t_0 (2.747165 s) is defined as the time of the first visible deviation from the (pre-crash) smooth temperature profile. Figures 7e and f show images during a later phase of the crash (time indicated in figure 7a), where poloidally localized structures (thought to be related to the ELM filaments observed by many other diagnostics) are seen to rotate poloidally (upward in the figure). To enhance these structures in the images, not the absolute (radiation) temperature, but $T_R - T_{R,av}$ is shown, where $T_{R,av}$ is the average temperature (calculated separately for each ECEI channel) after the ELM crash (shaded area in figure 7a). These filaments have a radiation temperature of about 200 eV.

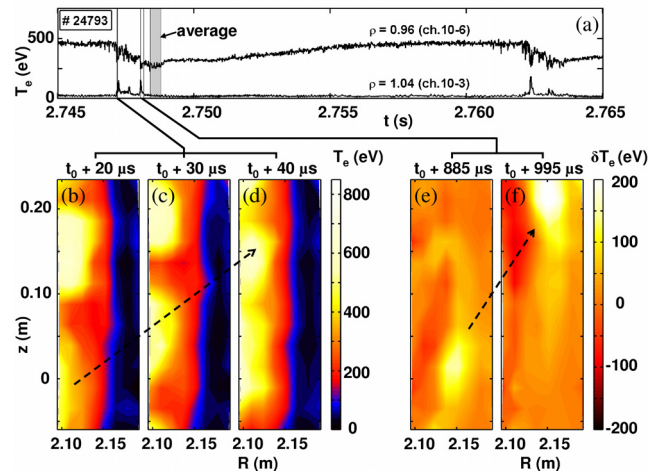


FIG. 7. (Color online). During an ELM crash, a pronounced 2D structure is observed at the plasma edge. The time traces in a) show a full ELM cycle. Images b), c) and d) show the ‘precursor’ phase, and images e) and f) show the movement of a ‘filament’. The arrows indicate the poloidal movement of the structures.

Whether one can interpret the observed filaments as electron temperature fluctuations depends upon the optical thickness of these structures. Figure 8c shows the optical thickness for typical electron density and temperature profiles (shown in figure 8a and b) at different phases during the ELM cycle. For both the pre-ELM and post-ELM cases, the optical thickness drops below unity at roughly the separatrix position, with rapidly rising values inside the separatrix. In the case where the electron temperature profile has been modified to include a filament (inspired by the radiation temperatures seen in figure 7e and f) but the electron density profile is left unchanged, it turns out that the optical thickness of this filament is roughly unity. The assumption of simultaneously increased density could drastically increase this

number. Consequently, the optical thickness is marginal (normally values above 2 to 3 are considered fully optically thick), but sufficiently large to assume the radiation temperature T_R is still comparable to the electron temperature T_e (note that $T_R \leq T_e$ so the actual temperature of the filaments might be higher).

Figure 8d shows the broadened emission profiles for the filament case. The red, solid line shows the cold resonance, and the dashed and dotted lines represent the (95%) boundaries of the broadened regions for ECEI and 1D ECE respectively. At low values of optical thickness, emission from the full broadened profile reaches the observer (re-absorption does not play a role), possibly reducing the radial resolution. However, in the region where the optical thickness is low, the width of the emitting layer is seen to be about 1cm. The radial resolution in these edge measurements is hence comparable to that of core measurements.

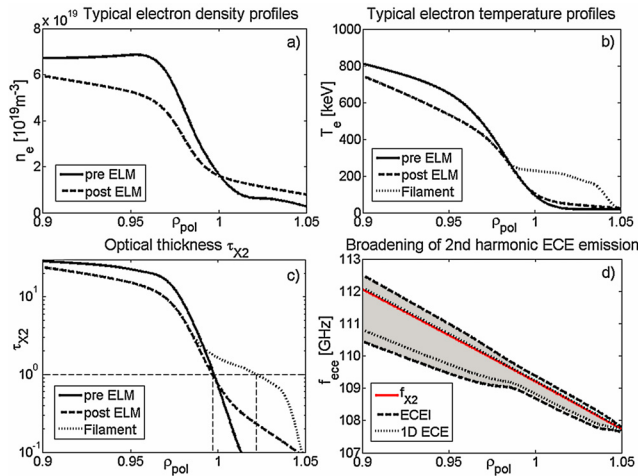


FIG. 8. (Color online). Typical profiles (based on measurements) of a) electron density, b) electron temperature and c) optical thickness just before and just after an ELM crash. Also the case with a simulated ‘filament’ is shown (filament only in temperature, not in density). The broadening of the second harmonic ECE resonance for the filament case is shown in d) for both ECEI and 1D ECE.

It should be noted that the effect of shinethrough¹³ (an increased radiation temperature just outside the separatrix, thought to be a non-local effect caused by downshifted radiation from further inside the plasma), often observed by the 1D ECE radiometer, has so far not been observed with ECEI. Although not fully understood, the difference might be explained by the different spot sizes of the two diagnostics (typically $w_\theta=15$ mm for ECEI and 35 mm for 1D ECE), resulting in a 2.5 times larger Doppler broadening for ECEI, and hence different emission profiles for both diagnostics (see figure 8d).

VI. SINGULAR VALUE DECOMPOSITION

The accuracy of the ECEI measurements is limited by thermal noise, inherent to all ECE diagnostics¹⁴. The (thermal) noise level is determined by the bandwidths of the system, and for ECEI at full sampling rate this amounts to a relative noise level of around 3%.

$$\sqrt{\langle dT_R^2 \rangle} / \langle T_R \rangle = \sqrt{2B_V / B_{IF}} \quad (2)$$

A distinctive advantage of a 2D system like ECEI is the fact that it provides many closely spaced data channels which, in many applications, will show similar data. This high degree of redundancy can be taken advantage of by using singular value decomposition (SVD) as a powerful tool for analyzing and filtering the 2D data. SVD is a well known mathematical technique to decompose 2-dimensional matrices into pairs of Eigenvectors. The mathematical details can be found in the literature¹⁵, but the general idea becomes clear by looking at the application of SVD for filtering ECEI data. In principle, ECEI data are 3-dimensional: there are 2 space dimensions, and a time dimension. However, for the SVD decomposition, we will regard ECEI data as having one time dimension (of length m , typically $m=1000$), and only one spatial dimension (of length $n=128$), treating the 16 by 8 two-dimensional space as a one-dimensional array of length 128. Therefore, the ECEI data are represented by a 2-dimensional m -by- n matrix X . The SVD decomposition of the data can now be written as:

$$X = USV^T \quad (3)$$

where U is an m -by- n matrix whose (length m) columns u_k represent time Eigenvectors (sometimes called ‘chronos’). V^T is an n -by- n matrix whose (length n) rows v_k^T represent spatial Eigenvectors (‘topos’). S is an n -by- n matrix whose only non-zero elements are on the diagonal, so $S=\text{diag}(s_1, \dots, s_k)$, where s_k , the so called singular values, are the Eigenvalues belonging to the topos-chronos pairs of Eigenvectors. By convention, the vectors are ordered from large to small s_k . Therefore, in the case of ECEI, the SVD results in 128 pairs of Eigenvectors (u_k and v_k^T) with corresponding decreasing Eigenvalues s_k . The filtered ECEI data X^l would then be represented by

$$X^l = \sum_{k=1}^l u_k s_k v_k^T \quad (4)$$

where l is the number of (most significant) Eigenvector pairs retained in the summation. The information contained in the Eigenvector pairs with $k>l$ is hence lost. Mathematically, X^l (the truncated SVD) is the closest rank l matrix to the original matrix X and is hence the best approximation to X , possible by only using l Eigenvector pairs.

SVD filtering has many aspects in common with Fourier decomposition. In Fourier decomposition however, the Eigenvectors are the harmonic functions, whereas in SVD these are replaced by the data specific topos-chronos pairs. If X can be described by a single Eigenvector pair, SVD will, unlike Fourier decomposition, find only one Eigenvector pair with non-zero Eigenvalue. Note that SVD filtering does hence not reduce the spatial or time resolution of the filtered data, as many other filtering methods (like Fourier filtering) do.

Coherent oscillations (present on multiple channels, with similar dynamics) will result in much larger singular values than incoherent (noise) oscillations. Therefore, the strong and coherent oscillations are still present in X^l , whereas the residue $X-X^l$ contains almost exclusively incoherent oscillations. This is of course only true if l is chosen sufficiently large, so that the coherent part of the data can be described by a rank l matrix. In practice, l is normally chosen to be between 10 and 20 in the analysis of ECEI data. For this purpose, the ECEI data are divided into data segments of typically 1000 time points. For

each of these segments the truncated SVD is calculated. The length of the segments is both determined by computational limits, and the requirement that the oscillations in the data do not show too large a time evolution (in which case more Eigenvector pairs would be needed to describe the dynamics, and the filtering would become less effective).

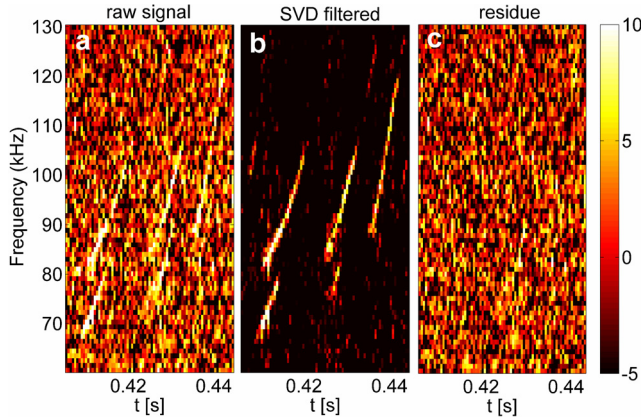


FIG. 9. (Color online). Singular value decomposition (SVD) filtering to remove (thermal) noise. In a), the spectrogram of the data of a single ECEI channel (channel 8-4, shot 25525) containing reversed shear Alfvén Eigenmodes (RSAEs) is shown. b) The same data after SVD filtering (truncated after 10 Eigenvector pairs) c) The residue which has been removed in the filtering.

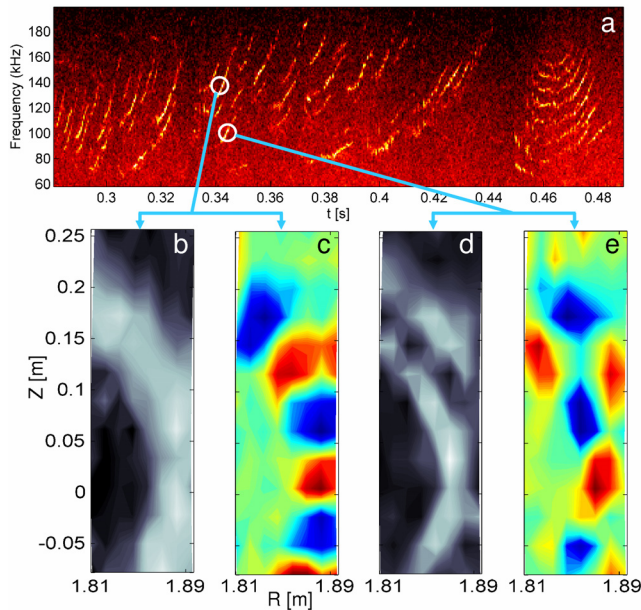


FIG. 10. (Color online). a) Spectrogram of shot 25528 showing many RSAEs. In b) and c) respectively the amplitude and mode structure of one of the RSAEs is shown. An example of an RSAE with a higher radial harmonic is shown in d) and e).

An example of SVD filtering is shown in figure 9. Shown are three spectrograms of the data from a single ECEI channel (channel 8-4, shot 25525) that contains Alfvén wave activity, so called reversed shear Alfvén Eigenmodes (RSAEs). These coherent oscillations have relative temperature fluctuation amplitudes of around 1%, and are hence below the thermal noise level. Figure 9a shows the spectrogram of the raw data (X).

Figure 9b shows the SVD filtered data (X^f , where $l=10$), and figure 9c shows the residue $X-X^f$. The color scaling for all three spectrograms is equal, so this clearly demonstrated that the SVD filtering significantly enhances the coherent information in the data, and the residue practically only contains noise. As in practice almost all oscillations of interest are at or below the thermal noise level, SVD filtering has proven to be almost essential for any direct plotting (stills or movies) of 2D ECEI data (like also the images in figure 7).

Figure 10 shows examples of the spatial structure of RSAEs as measured by ECEI. The Fourier amplitude in figure 10b and mode structure (or more accurately the real part of the complex Fourier amplitude) in 10c show a radially localized oscillation with a poloidal mode number of around $m=8$. An RSAE with a second radial harmonic is shown in figure 10d and e. This analysis made use of both SVD filtering to get rid of the majority of the noise, and subsequent Fourier frequency selection to pick out the separate modes. These first, local, 2D ECE measurements of the mode structure of Alfvén waves reveal more information than previous 1D measurements¹⁶, and could contribute to the understanding of these modes and the associated fast particle transport. Similar results have in the mean time been achieved with another ECEI system on DIII-D¹⁷.

¹H.K. Park, E. Mazzucato, T. Munsat, C.W. Domier, M. Johnson, N.C. Luhmann, Jr., J. Wang, I.G.J. Classen, A.J.H. Donné, and M.J. van de Pol, *Rev. Sci. Instrum.* **75**, 3787 (2004).

²H.K. Park, N.C. Luhmann, A.J.H. Donné, I.G.J. Classen, C.W. Domier, E. Mazzucato, T. Munsat, M.J. van de Pol, Z. Xia and TEXTOR team, *Phys. Rev. Lett.* **96**, 195003 (2006)

³H.K. Park, A.J.H. Donné, N.C. Luhmann, I.G.J. Classen, C.W. Domier, E. Mazzucato, T. Munsat, M.J. van de Pol, Z. Xia and TEXTOR team, *Phys. Rev. Lett.* **96**, 195004 (2006)

⁴I.G.J. Classen, E. Westerhof, C.W. Domier, A.J.H. Donné, R.J.E. Jaspers, N.C. Luhmann Jr., H.K. Park, M.J. van de Pol, G.W. Spakman, M.W. Jakubowski and TEXTOR team, *Phys. Rev. Lett.* **98**, 35001 (2007)

⁵G.W. Spakman, G.M.D. Hogeweij, R.J.E. Jaspers, F.C. Schüller, E. Westerhof, J.E. Boom, I.G.J. Classen, E. Delabie, C. Domier, A.J.H. Donné, M.Yu. Kantor, A. Krämer-Flecken, Y. Liang, N.C. Luhmann Jr, H.K. Park, M.J. van de Pol, O. Schmitz, J.W. Oosterbeek and the TEXTOR, Team, *Nucl. Fusion* **48** 115005 (2008)

⁶T. Munsat, C.W. Domier, X. Kong, T. Liang, N.C. Luhmann, Jr., B.J. Tobias, W. Lee, H.K. Park, G. Yun, I.G.J. Classen, and A.J.H. Donné, *Applied Optics* **49**, Iss. 19, pp. E20–E30 (2010)

⁷B. Tobias, X Kong, T. Liang, A. Spear, C.W. Domier, N.C. Luhmann, Jr, I.G.J. Classen, J.E. Boom, M.J. van de Pol, R. Jaspers, A.J.H. Donné, H.K. Park, and T. Munsat, *Rev. Sci. Instrum.* **80**, 093502 (2009).

⁸C.W. Domier, Z.G. Xia, P. Zhang, N.C. Luhmann, Jr., H.K. Park, E. Mazzucato, M.J. van de Pol, I.G.J. Classen, A.J.H. Donné, and R. Jaspers, *Rev. Sci. Instrum.* **77**, 10E924 (2006).

⁹P. Zhang, C.W. Domier, T. Liang, X. Kong, B. Tobias, N.C. Luhmann, Jr., H. Park, I.G.J. Classen, M.J. van de Pol, A.J.H. Donné, and R. Jaspers, *Rev. Sci. Instrum.* **79**, 10F103 (2008).

¹⁰M. Bornatici, *Plasma Physics* **24**, 629 (1982)

¹¹I.H. Hutchinson, ‘Principles of plasma diagnostics’, Cambridge University Press (1987)

¹²C. Watts, H.J. Hartfuss, M. Häse, *Rev. Sci. Instrum.* **75**, 3177 (2004).

¹³W. Suttrop, A.G. Peeters, IPP Report 1/306

¹⁴G. Bekefi, ‘Radiation processes in Plasmas’, New York, Wiley (1966).

¹⁵Strang G., *Introduction to Linear Algebra*. Wellesley, MA: Wellesley Cambridge Press, 1998

¹⁶M.A. Van Zeeland, G.J. Kramer, M.E. Austin, R.L. Boivin, W.W. Heidbrink, M.A. Makowski, G.R. McKee, R. Nazikian, W.M. Solomon, and G. Wang, *Phys. Rev. Lett.* **97**, 135001 (2006).

¹⁷B. Tobias, C.W. Domier, T. Liang, X. Kong, L. Yu, G.S. Yun, H.K. Park, I.G.J. Classen, J.E. Boom, A.J.H. Donné, T.L. Munsat, R. Nazikian, R.L. Boivin, and N.C. Luhmann, Jr., this conference